Analysis of Synchronverter Self-synchronization Dynamics to Facilitate Parameter Tuning

Shuan Dong, *Student Member, IEEE*, Jingya Jiang, *Student Member, IEEE*, and Yu Christine Chen, *Member, IEEE*

***Abstract*—This paper proposes a self-synchronizing synchronverter controller design that leverages the addition of a virtual resistance (along with a suitable coordinate transformation) to compute feedback signals during self synchronization prior to grid connection. With respect to analysis, we exploit separation-of-time-scales arguments and develop appropriate reduced-order models, which are well-suited for studying phase-angle and voltage-magnitude self-synchronization dynamics independently. Our work provides analytical justification for the effects of pertinent controller parameters and system initial conditions on self-synchronization dynamics observed empirically in time-domain simulations. As such, it offers practical guidance on favourable parameter-value settings to achieve fast self synchronization, and it yields accurate estimates for self-synchronization times with well-tuned parameters. Through numerical simulations and experiments, we illustrate the efficacy of the proposed controller design and verify the validity of subsequent analyses.**

***Index Terms*—Damping correction loop, dynamics, model-order reduction, self synchronization, synchronverter, virtual resistance, virtual synchronous generator.**

I. Introduction

DRIVEN by environmental considerations, renewable energy sources (RESs) are expected to displace a sizeable portion of conventional fossil fuel-based synchronous generators. Compared with these, converter-interfaced RESs have little or no inertia, so their large-scale integration significantly reduces total grid-wide inertia [1]. Also, conventional control strategies of RES converters rely on phase-locked loops (PLLs), which may cause instability, especially under weak-grid conditions [2]. To address these problems, the concept of the virtual synchronous generator (VSG) has been proposed, which enables the RES converter and its dc-side storage device to emulate synchronous-generator dynamics (see, e.g., [3]–[7]). Main advantages of VSGs are that they contribute more inertia to the grid, and because they are independent of PLLs during normal operation, they avoid PLL-related instability and enhance overall system performance.

A highly desirable property for the VSG to have is the so-called *self-synchronization* capability, which refers to the ability for the VSG to automatically synchronize its inner voltage to the grid-side voltage without PLLs before closing the breaker, as shown in Fig. 1 [8]. This capability helps to avoid potentially large start-up currents when physically connecting the VSG to the grid, and in turn, protects the power-electronic devices in the VSG. Moreover, if the VSG is not endowed with the self-synchronization capability, then a PLL is required to measure the grid-side voltage phase angle in order to synchronize the VSG voltage to that of the grid before physical connection [5], [6]. The self-synchronizing VSG completely obviates the need for a PLL in the controller and significantly simplifies the overall design. Specifically, compelling arguments for bypassing the PLL include past observations that PLL-based designs are associated with greater computational burden and more complex parameter tuning [8]–[12].

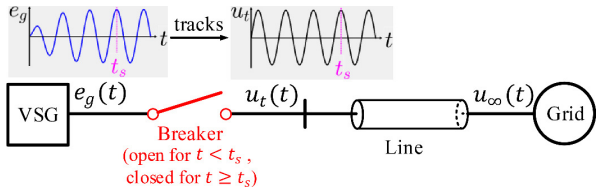

Fig. 1. Illustrative diagram of self synchronization. For $t < t_s$, the breaker is open, and the VSG automatically synchronizes its inner voltage $e_g(t)$ to the grid voltage $u_\infty(t) = u_t(t)$ without PLLs. For $t \geq t_s$, $e_g(t)$ and $u_t(t)$ are synchronized, and the breaker may close without causing large start-up currents after grid connection.

Owing to the value of self synchronization without relying on PLLs, numerous self-synchronizing VSG designs have been proposed in the literature [8], [13]–[15]. They typically adopt a virtual impedance, which is used to generate active- and reactive-power feedback signals during self synchronization. However, the virtual impedance requires simultaneous tuning of two parameters, i.e., resistance and reactance, which may be difficult. For example, [13] requires tuning of two sets of virtual-impedance values, a large one during self synchronization to reduce start-up currents and a small one for normal operation afterwards. Furthermore, in the method proposed in [16], the virtual-impedance value requires the solution of a system of inequality constraints constructed from a set of performance requirements. The designs in [8], [14], [15] use the virtual impedance during self synchronization and then bypass it immediately after grid connection. Improperly tuned impedance parameters may lead to slow or even unsuccessful self synchronization [17].

Our recent work in [18] proposes a self-synchronizing synchronverter[1] design that addresses the shortcomings above. Instead of the virtual impedance, [18] adopts a virtual resistance

S. Dong and Y. C. Chen are with the Department of Electrical and Computer Engineering at The University of British Columbia, Vancouver, BC, V6T 1Z4, Canada. Email: {shuan, chen}@ece.ubc.ca.

J. Jiang is with the Department of Electrical Engineering at the Beijing Jiaotong University, Beijing 100044, China. Email: jyjiang@bjtu.edu.cn.

[1]The synchronverter is a representative VSG design with concise structure [3].

with only one parameter (along with a suitable coordinate transformation) to provide the controller with active- and reactive-power feedback signals during self synchronization. Also, [18] uses the damping correction loop first proposed in [15] to adjust the system damping freely with only one additional parameter. These features enable the controller to be more easily tuned to achieve faster self synchronization than existing designs. However, self-synchronization dynamics are not thoroughly analyzed in [15] and [18]. They report only numerical results that demonstrate the effects of varying pertinent controller parameters on self-synchronization dynamics, but not those of different initial conditions. To the best of our knowledge, there are few existing analytical studies on self-synchronization dynamics. For example, [8] contains only qualitative descriptions for how certain parameters influence self synchronization, and [11] studies self-synchronization dynamics under various initial conditions but does not provide detailed system-theoretic analysis. Moreover, typically, previous studies (e.g., [8], [13]–[15], [18]) only evaluate self-synchronization time via numerical simulations instead of analysis for a general setting. In this work, analysis of self-synchronization dynamics yields convergence guarantees, facilitates parameter tuning, and reveals minimum time required to achieve synchronization.

This paper builds on the self-synchronizing controller design in [18] and provides extensions in several directions. First, via time-domain simulations, we empirically observe the impacts of controller parameters as well as system initial conditions on self-synchronization dynamics. Then we develop suitable reduced-order models to analyze the faster phase-angle self-synchronization dynamics and slower voltage-magnitude ones separately. These perspectives offer analytical justification for the effects of controller parameters and initial conditions on self-synchronization dynamics. They also provide accurate estimates for phase-angle and voltage-magnitude self-synchronization times. Moreover, building on the aforementioned analyses, we recommend practical parameter settings to achieve fast self synchronization. Finally, we validate the analyses performed based on the reduced-order models and verify parameter-value settings via numerical case studies and experiments.

The remainder of this paper is organized as follows. Section II describes the proposed synchronverter design and motivates the need to study self-synchronization dynamics. In Section III, we develop reduced-order models to analyze these dynamics in detail and further recommend parameter values to achieve fast synchronization. Then, Sections IV and V validate our self-synchronization dynamic analyses via time-domain simulations and experiments, respectively. Finally, concluding remarks and directions for future work are offered in Section VI.

II. Self-synchronizing Synchronverter Design

In this section, we describe the proposed synchronverter design, which was first reported in [18], and then motivate the need to analyze self-synchronization dynamics.

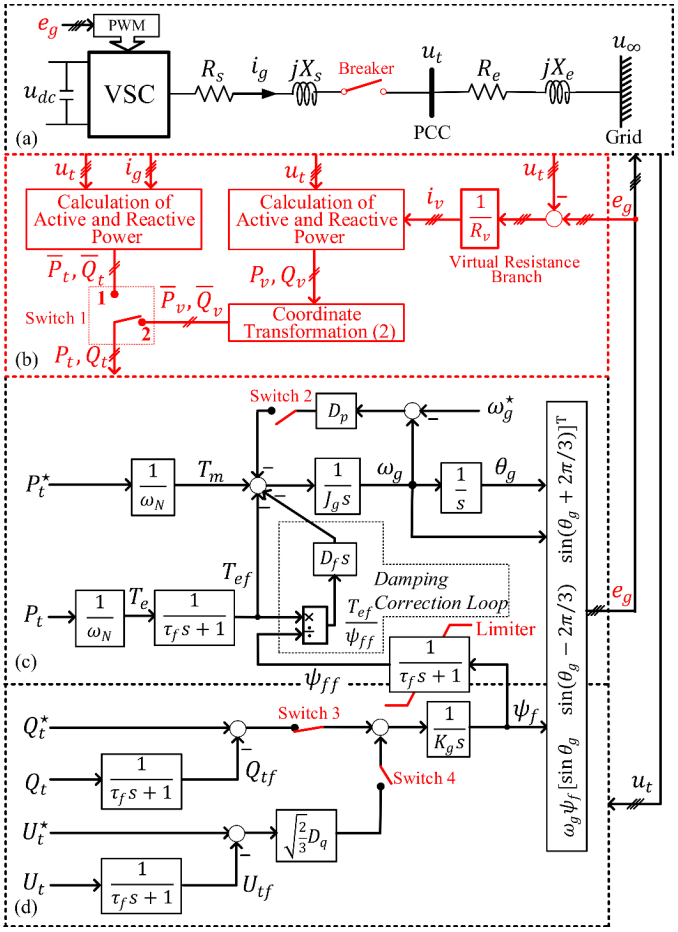

Fig. 2. Proposed self-synchronizing synchronverter [18], which has few parameters that require tuning. Highlighted in red colour are aspects of particular relevance to the proposed design. (a) Grid interface. (b) Power computation block. (c) Active-power loop. (d) Reactive-power loop.

A. Proposed Self-synchronizing Synchronverter Design

A voltage source converter (VSC), which is controlled via a synchronverter, is connected to the point of common coupling (PCC) with voltage u_t via an L-type filter $R_s + jX_s$ and a breaker, as shown in Fig. 2(a). The external grid, which is connected to the PCC, is modelled as a voltage source u_∞ behind impedance $R_e + jX_e$. The proposed controller comprises the power computation block, the active-power loop (APL), and the reactive-power loop (RPL), as shown in Figs. 2(b)–2(d), respectively. Below, we first focus on the power computation block, which includes the key design point, i.e., the virtual resistance, for self synchronization. Then, for completeness, we briefly describe the APL and RPL dynamical models. Note that the synchronverter inner voltage e_g is obtained by combining the rotating speed ω_g and rotor angle θ_g from the APL, as well as the excitation flux ψ_f from the RPL, and its corresponding voltage line-to-line RMS value is $E_g = \sqrt{3/2}\omega_g\psi_f$ [15].

1) Power Computation Block: In the power computation block, as shown in Fig. 2(b), we adopt a virtual resistance R_v instead of the typical virtual impedance $\widetilde{L}_v s + \widetilde{R}_v$. Unlike $\widetilde{L}_v s + \widetilde{R}_v$, which has two parameters that require tuning, R_v has only one. During self synchronization, the breaker in

Fig. 2(a) is open, and the actual synchronverter active- and reactive-power outputs, $\overline{P}_t$ and $\overline{Q}_t$, are both zero. The goal of self synchronization is to ensure that the inner voltage e_g closely tracks u_t, the measured PCC voltage, which is equal to the grid voltage u_∞ when the breaker is open. To achieve this, the power computation block provides the APL and RPL with feedback signals P_t and Q_t that result from their virtual analogues P_v and Q_v. By setting Switch 1 in Fig. 2(b) to position 2, we obtain virtual current i_v flowing through the virtual resistance R_v according to $i_v = (e_g - u_t)/R_v$. With i_v and u_t in place, we compute the virtual active and reactive powers, i.e., P_v and Q_v [18]. Let U_∞ and θ_∞ denote, respectively, the line-to-line RMS value and the phase angle of u_∞; and define $\theta_{g\infty} := \theta_g - \theta_\infty$ as the phase-angle difference between e_g and u_∞, then P_v and Q_v are given by

$$P_v = \frac{E_g U_\infty}{R_v}\cos\theta_{g\infty} - \frac{U_\infty^2}{R_v},\quad Q_v = -\frac{E_g U_\infty}{R_v}\sin\theta_{g\infty}, \quad (1)$$

respectively. Note that since we adopt a virtual resistance only, P_v and Q_v are, respectively, closely related to E_g and $\theta_{g\infty}$. However, the APL and RPL are designed for predominantly inductive grid conditions. In other words, the APL input P_t and RPL input Q_t are, respectively, regulated by the rotor angle θ_g and the inner voltage magnitude E_g (or the excitation flux ψ_f). Thus, during self synchronization, we cannot directly use P_v and Q_v as the APL and RPL inputs. In fact, linearization of a self-synchronization design that uses only the virtual resistance reveals a pair of eigenvalues in the right half-plane, so such a design is unstable. In view of this, we leverage the following coordinate transformation:

$$\begin{bmatrix}\overline{P}_v\\ \overline{Q}_v\end{bmatrix} = \begin{bmatrix}0 & -1\\ 1 & 0\end{bmatrix}\begin{bmatrix}P_v\\ Q_v\end{bmatrix}, \quad (2)$$

and instead use the post-transformation variables $\overline{P}_v$ and $\overline{Q}_v$ as the APL and RPL inputs, respectively, so that

$$P_t = \overline{P}_v = \frac{E_g U_\infty}{R_v}\sin\theta_{g\infty}, \quad (3)$$

$$Q_t = \overline{Q}_v = \frac{E_g U_\infty}{R_v}\cos\theta_{g\infty} - \frac{U_\infty^2}{R_v}. \quad (4)$$

In this way, the APL and RPL regulate, respectively, P_t and Q_t using θ_g and E_g (or ψ_f) during self synchronization. As shown in Fig. 3, via the coordinate transformation in (2), the virtual resistance R_v acts equivalently as a reactance for the purpose of computing virtual power feedback signals [18]. We also note that the proposed virtual-resistance design (together with the coordinate transformation in (2)) cannot be replaced by a virtual inductance $\widetilde{L}_v s$ only (i.e., by setting $\widetilde{R}_v$ to be zero in a virtual impedance branch $\widetilde{L}_v s + \widetilde{R}_v$). Via small-signal analysis, we find that the inductor dynamics introduced by $\widetilde{L}_v s$ present a pair of unstable eigenvalues that lead to unsuccessful self synchronization. These undesirable dynamics are bypassed in the proposed design via the *algebraic* coordinate transformation in (2).

2) Active- and Reactive-power Loops: During self synchronization, the APL (Fig. 2(c)) and RPL (Fig. 2(d)), respectively, synchronize the phase angle and the voltage magnitude of e_g to those of u_∞ by setting P_t and Q_t to zero. The APL

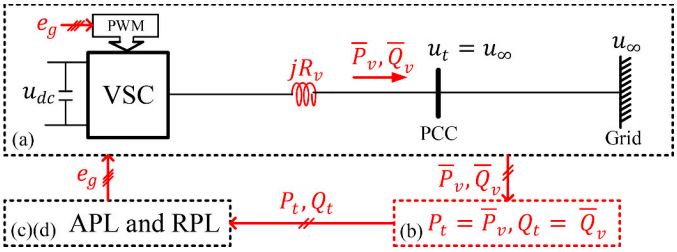

Fig. 3. Equivalent representation of proposed synchronverter design in Fig. 2 during self synchronization (Switch 1 in Fig. 2(b) is in position 2). (a) Equivalent grid interface corresponding to Figs. 2(a) and 2(b), in which R_v acts as virtual reactance jR_v due to the algebraic coordinate transformation in (2). (b) Active- and reactive-power feedback signals. (c)(d) APL and RPL.

regulates $\theta_{g\infty}$ to zero (phase-angle self synchronization), and the RPL regulates E_g to be U_∞ (voltage-magnitude self synchronization). Let S_i represent the state of Switch i, $i = 2, 3, 4$, i.e., $S_i = 1$ if Switch i is closed and $S_i = 0$ if Switch i is open. Then, the APL and RPL dynamics are described by

$$J_g\frac{d\omega_g}{dt} = \frac{P_t^\star}{\omega_N} - T_{ef} - S_2 D_p(\omega_g - \omega_g^\star) - D_f\frac{d}{dt}\left(\frac{T_{ef}}{\psi_{ff}}\right), \quad (5)$$

$$K_g\frac{d\psi_f}{dt} = S_3(Q_t^\star - Q_{tf}) + S_4\sqrt{\frac{2}{3}}D_q(U_t^\star - U_{tf}). \quad (6)$$

In (5), J_g denotes the inertia constant, $\omega_g^\star$ the reference value of ω_g, $P_t^\star$ the active-power reference, and ω_N the rated rotating speed. The term $S_2 D_p(\omega_g - \omega_g^\star)$ is the switchable power-frequency droop control; and the term $D_f\frac{d}{dt}\left(\frac{T_{ef}}{\psi_{ff}}\right)$ represents the damping correction loop, which adjusts the APL damping freely [15]. Furthermore, by integrating ω_g over time, we get the rotor angle, i.e., $\theta_g(t) = \int_0^t \omega_g(\tau)d\tau$. In (6), K_g is a tuneable parameter, which determines the RPL response speed; $Q_t^\star$ and $U_t^\star$ are, respectively, the reference value of Q_t and the line-to-line RMS value U_t of u_t; and the term $S_4\sqrt{\frac{2}{3}}D_q(U_t^\star - U_{tf})$ represents the switchable voltage-droop control. In (5) and (6), T_{ef}, ψ_{ff}, Q_{tf}, and U_{tf} are filtered signals obtained from

$$\tau_f\frac{dT_{ef}}{dt} = -T_{ef} + T_e, \quad \tau_f\frac{d\psi_{ff}}{dt} = -\psi_{ff} + \psi_f, \quad (7)$$

$$\tau_f\frac{dQ_{tf}}{dt} = -Q_{tf} + Q_t, \quad \tau_f\frac{dU_{tf}}{dt} = -U_{tf} + U_t, \quad (8)$$

where τ_f is the time constant of low-pass filters (LPFs), and $T_e = P_t/\omega_N$ is the electromagnetic torque. Since ψ_{ff} is in the denominator in (5), we also include a limiter on ψ_{ff}, ensuring that $\psi_{ff} > 0$. During self synchronization, we set $S_2 = 0$ and $P_t^\star = 0$, so that $P_t = \overline{P}_v$ regulates to zero. Then, according to (3), we get $\theta_{g\infty} = 0$ and thus achieve phase-angle self synchronization. Also, we close Switch 3 ($S_3 = 1$), open Switch 4 ($S_4 = 0$), and set $Q_t^\star = 0$. In this way, we regulate $Q_t = \overline{Q}_v$ to be zero, as desired.

Remark 1. By examining (3) and (4), we note that phase-angle self synchronization ought to be achieved earlier than that of the voltage magnitude. Only after the APL regulates $\theta_{g\infty}$ to be zero (or $2k\pi$, $k \in \mathbb{Z}$) can we get $E_g = U_\infty$ when $Q_t = 0$. Otherwise, according to (4), the RPL would regulate E_g to be $U_\infty/\cos\theta_{g\infty}$, which would not be desired. ■

Once e_g synchronizes with u_∞, we close the breaker and set Switch 1 to position 1. At this point, the synchronverter is connected to the grid and operates normally. During normal operation, the feedback active and reactive powers are the actual converter outputs $\overline{P}_t$ and $\overline{Q}_t$, as shown in Fig. 2(b).

3) Full-order Dynamical Model: Suitable algebraic manipulation of (3)–(8), along with appropriate switch settings, result in the following sixth-order nonlinear model describing system dynamics during self synchronization:

$$\frac{d\theta_{g\infty}}{dt} = \omega_{g\infty}, \tag{9}$$

$$\frac{d\omega_{g\infty}}{dt} = -D_f\sqrt{\frac{3}{2}}\frac{(\omega_\infty+\omega_{g\infty})\psi_f U_\infty}{J_g\tau_f\omega_N R_v\psi_{ff}}\sin\theta_{g\infty} + \left(D_f\frac{\psi_f}{\tau_f\psi_{ff}^2}-1\right)\frac{T_{ef}}{J_g}, \tag{10}$$

$$\frac{dT_{ef}}{dt} = \sqrt{\frac{3}{2}}\frac{(\omega_\infty+\omega_{g\infty})\psi_f U_\infty}{\tau_f\omega_N R_v}\sin\theta_{g\infty} - \frac{1}{\tau_f}T_{ef}, \tag{11}$$

$$\frac{d\psi_f}{dt} = -\frac{1}{K_g}Q_{tf}, \tag{12}$$

$$\frac{dQ_{tf}}{dt} = \sqrt{\frac{3}{2}}\frac{(\omega_\infty+\omega_{g\infty})\psi_f U_\infty}{\tau_f R_v}\cos\theta_{g\infty} - \frac{U_\infty^2}{\tau_f R_v} - \frac{Q_{tf}}{\tau_f}, \tag{13}$$

$$\frac{d\psi_{ff}}{dt} = \frac{1}{\tau_f}\left(\psi_f-\psi_{ff}\right), \tag{14}$$

where ω_∞ is the angular-speed of u_∞, and $\omega_{g\infty} := \omega_g - \omega_\infty$ is the angular speed difference between e_g and u_∞. In the model described by (9)–(14), (10) is obtained by substituting (3) and (7) into (5), (11) is obtained by substituting (3) into the first expression in (7), (12) is obtained by setting $S_3 = 1$ and $S_4 = 0$ in (6), and (13) is obtained by substituting (4) into the first expression in (8). To simplify notation, let x denote the state vector, i.e., $x = [\theta_{g\infty}, \omega_{g\infty}, T_{ef}, \psi_f, Q_{tf}, \psi_{ff}]^{\mathrm{T}}$.

By setting (9)–(14) to zero and solving them (recall that $\psi_{ff} > 0$), we find that the system has a family of equilibrium points x°, as follows:

$$x^\circ = \left[2k\pi,\ 0,\ 0,\ \sqrt{\frac{2}{3}}\frac{U_\infty}{\omega_\infty},\ 0,\ \sqrt{\frac{2}{3}}\frac{U_\infty}{\omega_\infty}\right]^{\mathrm{T}} =: [\theta_{g\infty}^\circ,\ \omega_{g\infty}^\circ,\ T_{ef}^\circ,\ \psi_f^\circ,\ Q_{tf}^\circ,\ \psi_{ff}^\circ]^{\mathrm{T}}, \tag{15}$$

where $k \in \mathbb{Z}$. Thus, self synchronization is achieved when x converges to x°. With regard to initial conditions, since the grid-voltage phase angle θ_∞ is unknown to the controller, the initial phase-angle difference $\theta_{g\infty}(0) \in (-\pi, \pi)$ rad. Remaining state variables in x can be initialized within the controller, e.g., we set $\omega_g(0) = \omega_N \approx \omega_\infty$, so that $\omega_{g\infty}(0) \approx 0$. Under these initial conditions, $\theta_{g\infty}(t)$ indeed converges to zero upon successful self synchronization, as desired.

B. Dynamic Response of Self Synchronization

The controller design described above is able to synchronize e_g to u_∞ before physical grid connection. In [18], we observe that tuning parameters D_f and K_g, respectively, affects phase-angle and voltage-magnitude self-synchronization dynamics. Next, via a numerical example, we show that while increasing D_f accelerates phase-angle self synchronization, there exists an upper bound to the $\theta_{g\infty}(t)$-convergence speed. We also show that while decreasing K_g accelerates voltage-magnitude self synchronization, sufficiently small K_g values result in undesirable transient overshoots.

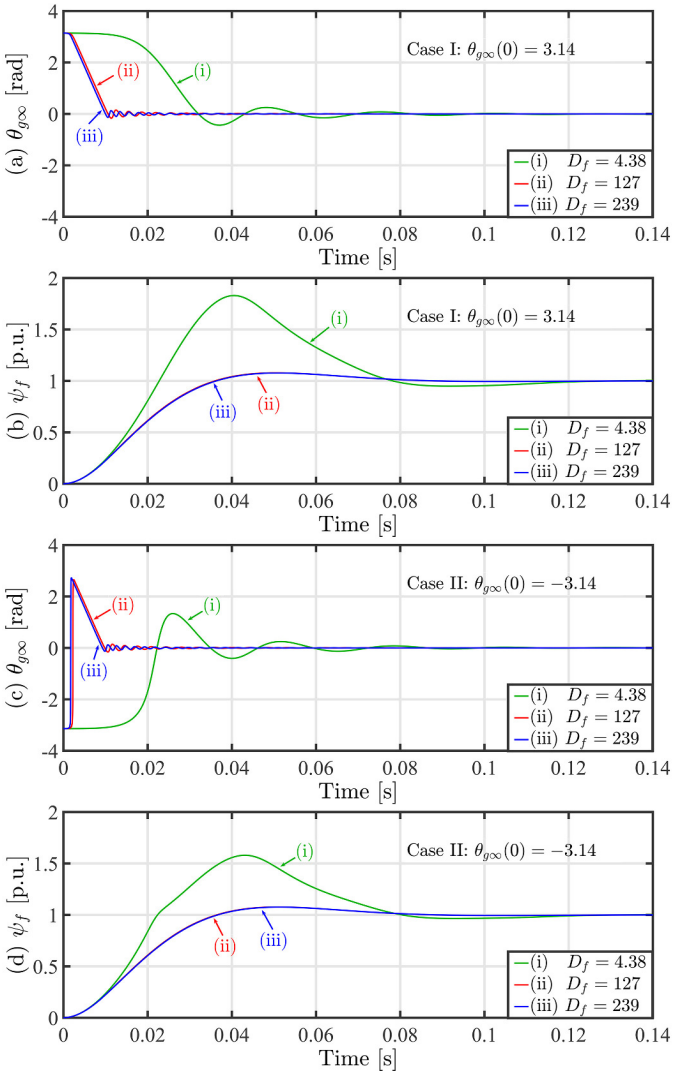

Fig. 4. Impacts of D_f on phase-angle self-synchronization dynamics. We find that: (i) increasing D_f accelerates the APL response speed and enables $\theta_{g\infty}(t)$ to converge to $\theta_{g\infty}^\circ$ more quickly, but there is an upper bound to phase-angle self-synchronization speed, (ii) reduced phase-angle self-synchronization speed results in slower voltage-magnitude self synchronization. (a)(b) Self-synchronization dynamics with $\theta_{g\infty}(0) = 3.14$ rad. (c)(d) Self-synchronization dynamics with $\theta_{g\infty}(0) = -3.14$ rad.

Example 1 (Impacts of D_f and K_g on Self Synchronization)**.** In this example, we simulate the synchronverter-connected system in Fig. 2 and observe the impacts of D_f and K_g on self-synchronization dynamics in three scenarios (Cases I–III). Other relevant parameter values are fixed as follows: $R_s = 0.741\ \Omega$, $L_s = 20$ mH, $R_e = 0\ \Omega$, $L_e = 38.5$ mH, $S_2 = 0$, $S_3 = 1$, $S_4 = 0$, $\tau_f = 0.01$ s, $R_v = 5\ \Omega$, $J_g = 11.2$ kg$\cdot$m^2, $\omega_N = \omega_g^\star = \omega_\infty = 376.99$ rad/s, $U_\infty = 6.60$ kV, $u_{dc} = 13$ kV, rated ac side voltage $U_N = 6.60$ kV, and rated synchronverter capacity $S_N = 1$ MVA. All simulations

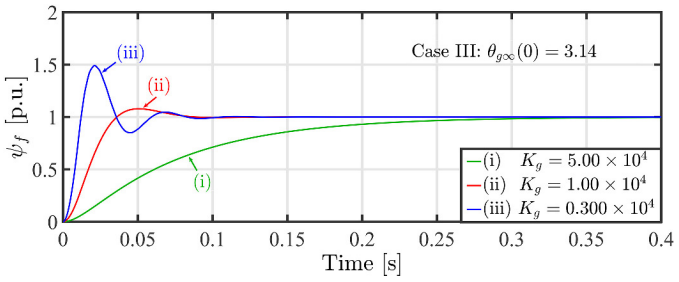

Fig. 5. Impacts of K_g on voltage-magnitude self-synchronization dynamics with $\theta_{g\infty}(0) = 3.14 \in (0, \pi)$ rad. We find that decreasing K_g accelerates the RPL response speed so that $\psi_f(t)$ converges to 1 p.u. more quickly, but sufficiently small K_g results in transient overshoots in $\psi_f(t)$.

are initialized at $\omega_{g\infty}(0) = 0$ rad/s, $T_{ef}(0) = 0$ N $\cdot$ m, $Q_{tf}(0) = 0$ Var, and $\psi_f(0) = \psi_{ff}(0) = 0.01$ Wb.

In Cases I and II, we observe effects of varying D_f on self-synchronization dynamics by setting $D_f = 4.38,\ 127,\ 239$ V $\cdot$ s^2/rad, as shown in Fig. 4 by traces marked as (i), (ii), and (iii), respectively. Furthermore, in order to discern the impacts of $\theta_{g\infty}(0)$ on self synchronization, we set $\theta_{g\infty}(0)$ to be 3.14 and -3.14 rad, respectively, in Cases I (shown in Figs. 4(a)–4(b)) and II (shown in Figs. 4(c)–4(d)). Here, we make two key observations. First, in both Cases I and II, increasing D_f from 4.38 to 127 V $\cdot$ s/rad results in $\theta_{g\infty}(t)$ converging to zero more quickly. This is because larger D_f corresponds to greater APL damping, which helps to accelerate the $\theta_{g\infty}(t)$-convergence rate. However, further increasing D_f to 239 V $\cdot$ s/rad does not lead to even faster phase-angle self synchronization. In fact, we find that with $D_f > 127$ V $\cdot$ s/rad, if $\theta_{g\infty}(0) = 3.14$ rad, $\theta_{g\infty}(t)$ converges to zero with speed near $-\omega_\infty$; and if $\theta_{g\infty}(0) = -3.14$ rad, $\theta_{g\infty}(t)$ first jumps to a positive value, and then also converges to zero with speed near $-\omega_\infty$. Moreover, by comparing traces (i), (ii), and (iii) in Figs. 4(b) and 4(d), we observe that $\psi_f(t)$ converges to 1 p.u. more slowly with much lower rate of $\theta_{g\infty}(t)$ convergence. This is consistent with Remark 1, as the RPL cannot track $E_g(t)$ to U_∞ (or $\psi_f(t)$ to 1 p.u.) until the APL has regulated $\theta_{g\infty}(t)$ to zero.

In Case III, we observe the impacts of K_g on self synchronization by setting $K_g = 5.00 \times 10^4,\ 1.00 \times 10^4,\ 0.300 \times 10^4$ Var $\cdot$ rad/V. Additionally, we set $D_f = 32.1$ V $\cdot$ s^2/rad and $\theta_{g\infty}(0) = 3.14$ rad. Here, we make another important observation. As shown in Fig. 5, decreasing K_g from 5.00×10^4 to 1.00×10^4 Var $\cdot$ rad/V causes $\psi_f(t)$ to converge to 1.00 p.u. more quickly, and thus accelerates voltage-magnitude self synchronization. However, choosing even smaller $K_g = 0.300 \times 10^4$ Var $\cdot$ rad/V does not further improve voltage-magnitude self-synchronization speed; instead, it causes undesirable transient overshoots in $\psi_f(t)$. Furthermore, setting $\theta_{g\infty}(0)$ to any other value gives rise to nearly identical simulation results as those shown in Fig. 5. ■

As highlighted via Example 1, for the self-synchronizing synchronverter controller described in Section II-A, we can accelerate phase-angle and voltage-magnitude self synchronization by increasing D_f and decreasing K_g, respectively, but only up to a certain limit. Next, we offer analytical justification for the empirical observations made in Example 1.

III. Analysis of Self-synchronization Dynamics

This section provides analytical insight into self-synchronization dynamics by studying the system in (9)–(14). Key to our analysis is the observation that, in practical settings and with well-tuned parameters D_f and K_g, phase-angle self synchronization is much faster than that of the voltage magnitude (see, e.g., Remark 1 and Fig. 4). This phenomenon uncovers a natural separation of time scales, which we leverage to construct two different reduced-order models that can be used to study phase-angle and voltage-magnitude self-synchronization dynamics independently. Then, based on our analyses, we recommend practical parameter settings that achieve fast self synchronization under various initial conditions.

A. Phase-angle Self-synchronization Dynamics

In order to approximate APL dynamics with a reduced-order model, we note that phase-angle self synchronization is achieved more quickly than voltage-magnitude self synchronization. Critical to the development of this reduced-order model are the following assumptions.

Assumption 1. We assume that $D_f \gg \tau_f \psi_f^\circ$ for a well-tuned self-synchronizing synchronverter. This assumption rests upon the fact that, if $D_f > \tau_f \psi_f^\circ$, the equilibrium points in (15) are exponentially stable for the linear system obtained by linearizing (9)–(14) around x°. We deduce this by applying the Routh-Hurwitz criterion (see, e.g., [19]) on the linearized system characteristic equation, which is given by

$$\left(\lambda^3 + \frac{1}{\tau_f}\lambda^2 + \sqrt{\frac{3}{2}}\frac{D_f \omega_\infty U_\infty}{J_g R_v \tau_f \omega_N}\lambda + \frac{{U_\infty}^2}{J_g R_v \tau_f \omega_N}\right) \cdot \left(\lambda + \frac{1}{\tau_f}\right) \cdot \left(\lambda^2 + \frac{1}{\tau_f}\lambda + \sqrt{\frac{3}{2}}\frac{\omega_\infty U_\infty}{K_g R_v \tau_f}\right) = 0. \quad (16)$$

Since x° is an exponentially stable equilibrium point for the linearized system under the condition that $D_f > \tau_f \psi_f^\circ$, this also guarantees that x° is exponentially stable for the nonlinear system in (9)–(14) near x° (see, e.g., Theorem 4.13 in [20]). Moreover, numerical results obtained in Example 1 indicate that larger D_f values would speed up phase-angle self synchronization, hence $D_f \gg \tau_f \psi_f^\circ$ for a well-tuned synchronverter is a reasonable assumption. ■

Assumption 2. Since state variables ψ_f and ψ_{ff} are associated with slower voltage-magnitude self-synchronization dynamics, we assume that $\frac{\psi_f(t)}{\psi_{ff}(t)} = c$ is a constant during time scales that are relevant to phase-angle self synchronization. ■

With the above assumptions in place, we approximate APL dynamics in (9)–(11) by a reduced second-order nonlinear model (a derivation is provided in Appendix A), which consists of (9) and

$$\frac{d\omega_{g\infty}}{dt} = -\frac{c}{\tau_f}\left(\alpha(\omega_\infty + \omega_{g\infty})\sin\theta_{g\infty} + \omega_{g\infty}\right), \quad (17)$$

where c and α are, respectively, given by

$$c = \frac{\psi_f}{\psi_{ff}}, \quad \alpha = \sqrt{\frac{3}{2}} \cdot \frac{D_f}{J_g} \cdot \frac{U_\infty}{\omega_N R_v}. \quad (18)$$

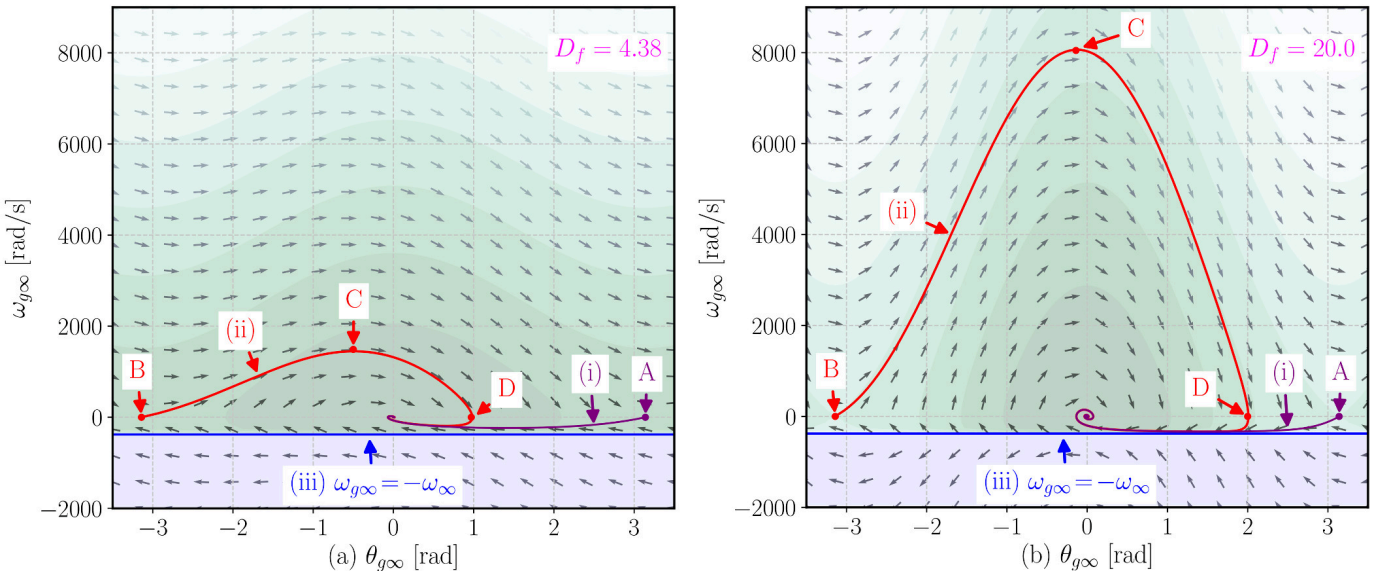

Fig. 6. Phase portrait of the reduced-order APL model consisting of (9) and (17). Trajectories marked as (i) and (ii) approach but do not cross the boundary delineated by $\omega_{g\infty} = -\omega_\infty$ (traces marked as (iii)), so $\frac{d\theta_{g\infty}}{dt} > -\omega_\infty$ during phase-angle self synchronization. (a) $D_f = 4.38$. (b) $D_f = 20.0$.

Note that tuneable parameters D_f and J_g both appear in the expression for α. For ease of parameter tuning, we set J_g to be the value tuned for normal operation and only vary D_f [18]. In this reduced-order model, state variables may take initial values $\theta_{g\infty}(0) \in (-\pi, \pi)$ rad and $\omega_{g\infty}(0) = 0$. We construct phase portraits of dynamic trajectories arising from all possible initial conditions in Fig. 6.

Via visual inspection of Fig. 6, we note that with $\theta_{g\infty}(0) \in (0, \pi)$ rad, as D_f increases from 4.38 (Fig. 6(a)) to 20.0 V $\cdot$ s/rad (Fig. 6(b)), the corresponding phase trajectories (see, e.g., trace (i) corresponding to $\theta_{g\infty}(0) = 3.14$ rad at the point A) get closer to, but remain above, the boundary delineated by trace (iii) corresponding to $\omega_{g\infty} = -\omega_\infty$. This offers analytical justification for the first observation in Example 1, where we note that increasing D_f amplifies the rate of convergence of $\theta_{g\infty}(t)$ to zero, up to an upper limit. Particularly, during phase-angle self synchronization, $\frac{d\theta_{g\infty}(t)}{dt} = \omega_{g\infty}(t) > -\omega_\infty$, for all $t > 0$. This is evident by checking that for all points along trace (iii) in Fig. 6, i.e., $\omega_{g\infty} = -\omega_\infty$, (17) can be simplified as

$$\left.\frac{d\omega_{g\infty}}{dt}\right|_{\omega_{g\infty}=-\omega_\infty} = \frac{c}{\tau_f} \cdot \omega_\infty > 0. \tag{19}$$

Treating $c > 0$ as a constant based on Assumption 2 and Appendix A, for all points along trace (iii), $\omega_{g\infty}$ grows larger, i.e., trajectories do not cross boundary (iii) from above. Furthermore, since D_f does not appear in (19), we find that as observed in Example 1, regardless of how large a value D_f takes, the rate of $\theta_{g\infty}(t)$ convergence approaches but does not exceed $-\omega_\infty$.

With initial conditions $\theta_{g\infty}(0) \in (-\pi, 0)$ rad, the phase portraits in Fig. 6 first reveal large positive $\omega_{g\infty}$ values before trajectories eventually converge to the origin. As an example, consider trace (ii) in Fig. 6(a), which corresponds to the phase trajectory arising from initial condition $\theta_{g\infty}(0) = -3.14$ rad, i.e., point B. The trajectory first climbs to point C corresponding to large positive $\omega_{g\infty}$ value, then reaches point D with positive phase-angle value, before finally converging to the origin in a similar fashion as the trajectory marked by trace (i). By comparing traces marked as (ii) in Figs. 6(a) and 6(b), we note that increasing D_f causes larger initial excursions in $\omega_{g\infty}(t)$. This explains the phenomenon observed in Example 1 (specifically in Fig. 4(c)), where $\theta_{g\infty}(t)$ jumps to a positive value before converging to zero with the choice of large D_f. Via numerical fitting, we can express the phase-angle self-synchronization time T_A with sufficiently large D_f as

$$T_\text{A} = \frac{|\theta_{g\infty}(0)|}{\omega_\infty} + \epsilon, \tag{20}$$

where ϵ represents an approximation error, which decreases as D_f increases.

B. Voltage-magnitude Self-synchronization Dynamics

To analyze voltage-magnitude self-synchronization dynamics, we assume that the faster phase-angle self-synchronization dynamics have reached steady state. Accordingly, we set $\omega_{g\infty} = 0$ and $\theta_{g\infty} = 0$ in (13) to get

$$\frac{dQ_{tf}}{dt} = \sqrt{\frac{3}{2}}\frac{\omega_\infty \psi_f U_\infty}{\tau_f R_v} - \frac{U_\infty^2}{\tau_f R_v} - \frac{Q_{tf}}{\tau_f}. \tag{21}$$

The system consisting of (12) and (21) represents an approximate reduced-order RPL model, which is decoupled from the faster APL dynamics. This RPL model is a linear system that can be analyzed via its transfer function. To this end, we take the Laplace transformation of (12) and (21), and solve the resultant for $\psi_f(s)$ as

$$\psi_f(s) = \frac{\omega_n^2}{s^2 + 2\zeta\omega_n s + \omega_n^2} \cdot \psi_f^\star =: G_\psi(s) \cdot \psi_f^\star, \tag{22}$$

where natural frequency ω_n and damping ratio ζ are given by

$$\omega_n = \sqrt{\sqrt{\frac{3}{2}}\frac{\omega_\infty U_\infty}{K_g \tau_f R_v}}, \quad \zeta = \sqrt{\frac{\sqrt{6}}{12}\frac{K_g R_v}{\omega_\infty U_\infty \tau_f}}, \tag{23}$$

respectively, and $\psi_f^\star = \sqrt{2/3}U_\infty/\omega_\infty = 1$ p.u. According to (23), decreasing K_g reduces the RPL damping ratio ζ. Indeed, as shown in Fig. 5, decreasing K_g from 5.00×10^4 (trace (i)) to 1.00×10^4 Var $\cdot$ rad/V (trace (ii)) causes voltage-magnitude synchronization to take less time. However, further decreasing K_g to 0.300×10^4 Var $\cdot$ rad/V (trace (iii)) results in an underdamped system, which would lead to transient overshoots in the $\psi_f(t)$ trajectory. We also note that the transfer function $G_\psi(s)$ is independent of initial condition $\theta_{g\infty}(0)$. This explains the final observation in Example 1 that $\theta_{g\infty}(0)$ has little to no influence on the dynamic response of $\psi_f(t)$.

C. Parameter Values to Achieve Fast Self Synchronization

To begin, we tune the virtual resistance R_v in the power computation block to a value with similar magnitude as the total reactance $X_t := X_s + X_e$. Particularly, we choose R_v as

$$R_v = 0.15 \cdot \frac{U_N^2}{S_N}, \tag{24}$$

where U_N and S_N, respectively, denote the rated voltage and capacity of the synchronverter. Next, recall that as observed in Example 1, significantly slower phase-angle self synchronization causes delays in voltage-magnitude self synchronization. In order to achieve fast phase-angle self synchronization, we recommend the following value of D_f:

$$D_f = \eta \cdot J_g \frac{\omega_N U_N}{S_N}, \tag{25}$$

where J_g is tuned for normal operation (i.e., after grid connection) using the method proposed in [21] and η is a tuneable coefficient. The choice of $\eta \geq 0.4$ ensures that D_f is sufficiently large to achieve fast phase-angle self synchronization, so as to satisfy Assumption 1 and justify the separation-of-time-scales arguments that led to the development of the reduced-order APL and RPL models in Sections III-A and III-B. This aspect is detailed in Appendix B. At the other extreme with $\eta = 6$, $\epsilon \approx 0.002$ s in (20), which is reasonably small. Although larger D_f leads to faster APL synchronization, the practical choice of D_f is limited by the processor sampling time T_s. As shown in Appendix C, setting D_f to be too large leads to instability when the synchronverter is implemented in discrete time, and the maximum allowable D_f depends on T_s. In typical implementations with $T_s = 50$ μs, we recommend setting $\eta = 0.6$ to strike a balance between ensuring system stability and achieving reasonably fast APL synchronization. If the sampling time is smaller, we may increase η to further accelerate the phase-angle self synchronization. Next, based on the analysis in Section III-B, we set the desired damping ratio in (23) to be $\zeta = 1/\sqrt{2}$, so that short settling time is achieved while avoiding large transient overshoots. Then, we compute K_g as

$$K_g = \frac{\sqrt{6}\tau_f \omega_\infty U_\infty}{R_v}. \tag{26}$$

With the choices outlined in (24) and (26), along with setting $\tau_f = 0.01$ s to guarantee the LPFs' noise rejection ability [15], the expected RPL settling time is [19]

$$T_{\mathrm{R}} = \frac{4}{\zeta \omega_n} = 8\tau_f = 0.08 \text{ s}, \tag{27}$$

where the second equality above results by substituting (23). In fact, with the parameter settings in (24)–(26), we can prove the self-synchronization capability of the proposed controller via stability analysis of the reduced-order APL and RPL models. Interested readers may refer to Appendix D for details.

IV. Simulation Verification

Via computer simulations in PSCAD/EMTDC, we verify the analyses and the recommended parameter settings from Section III. We also validate that the reduced second-order nonlinear APL model accurately reflects phase-angle self-synchronization dynamics. Since the ideas presented in Section III can be readily validated for the system used in Example 1 by examining Figs. 4 and 5, here, we opt for a different set of system parameters, as follows: $R_s = 1.62$ Ω, $L_s = 43$ mH, $R_e = 1.51$ Ω, $L_e = 40$ mH, $\omega_N = \omega_g^\star = \omega_\infty = 376.99$ rad/s, $U_N = U_\infty = 13.8$ kV, $u_{dc} = 25$ kV, and $S_N = 2$ MVA.

A. Verification of Self-synchronization Analysis

Using the parameter tuning method in [21] customized for normal operation (i.e., after grid connection), we first choose $J_g = 34.0$ kg $\cdot$ m^2. Then, according to (24), (25), and (26), we compute synchronverter parameters during self synchronization (i.e., before grid connection) and obtain $R_v = 14.3$ Ω, $D_f = 531$ V $\cdot$ s^2/rad, and $K_g = 8.92 \times 10^3$ Var $\cdot$ rad/V. In our simulations, the solution time step (which is analogous to controller sampling time in practice) is very small (1 μs), so setting $\eta = 6$ does not destabilize the system. With the above parameter values, we simulate the synchronverter-connected system in Fig. 2 in PSCAD/EMTDC with initial phase-angle difference $\theta_{g\infty}(0) = -3.14, 0, 3.14$ rad. In all cases, the synchronverter begins self synchronization at $t = 0$ s and reaches steady state before $t = 0.15$ s. At this point, we close the breaker, set Switch 1 from position 2 to 1, and fix $D_f = 2.17$ V $\cdot$ s^2/rad to begin normal operation.

Key simulation results are plotted in Fig. 7. As shown in Fig. 7(a) by traces (i) and (iii) respectively, $\theta_{g\infty}(t)$ converges to nearly zero at $T_{\mathrm{A}} \approx 0.01$ s for both $\theta_{g\infty}(0) = -3.14, 3.14$ rad. This agrees well with the phase-angle self-synchronization time predicted in (20), and it also validates the effectiveness of the choice of D_f recommended in (25). Moreover, as shown in Fig. 7(b), the actual $\psi_f(t)$ trajectories arising from all phase-angle initial conditions (traces (i)–(iii)) nearly overlap with the step response of $G_\psi(s)$ in (22) (trace (iv)). The settling time for all $\psi_f(t)$ trajectories shown as traces (i)–(iii) in Fig. 7(b) is $T_{\mathrm{R}} \approx 0.08$ s, as predicted in (27). Moreover, varying the initial condition $\theta_{g\infty}(0)$ does not significantly affect $\psi_f(t)$, as expected from the analysis performed in Section III-B. Thus, simulation results shown in Fig. 7(b)

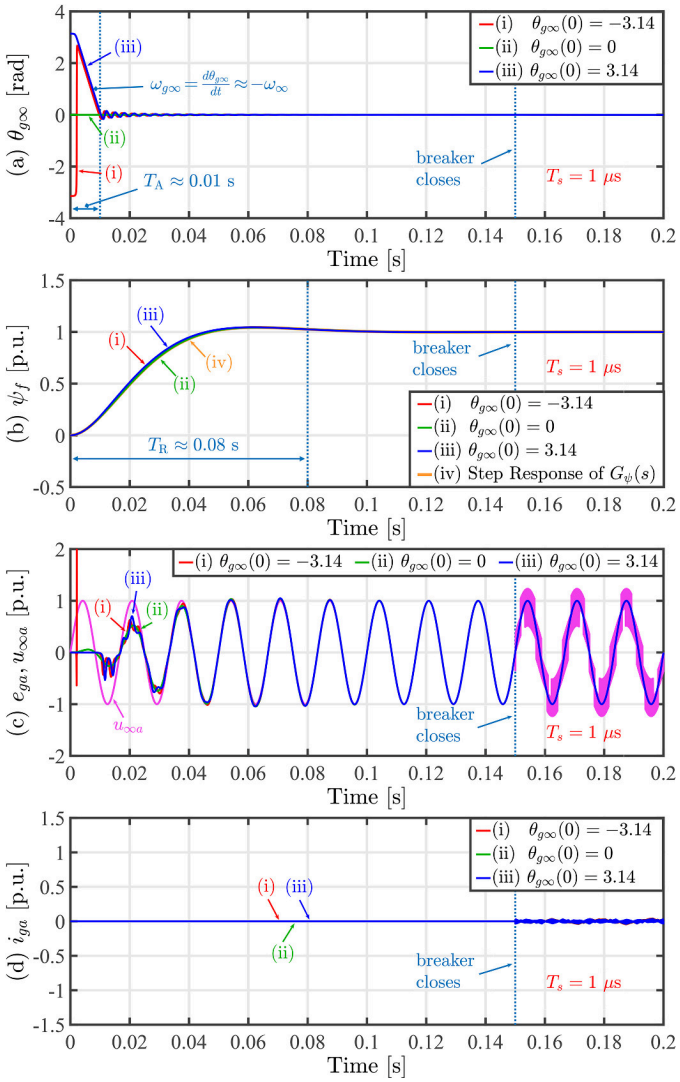

Fig. 7. Self-synchronization simulation results using the proposed controller design. These verify our analyses of self-synchronization dynamics, which leverage two suitable reduced-order models to study phase-angle and voltage-magnitude dynamics independently, as detailed in Section III.

verify the reduced-order RPL model and subsequent analysis for voltage-magnitude self-synchronization dynamics, as well as the parameter settings given by (24) and (26). By comparing Figs. 7(a) and 7(b), we note that there indeed exists a separation of time scales between phase-angle and voltage-magnitude dynamics. Particularly, $\theta_{g\infty}(t)$ converges to zero very quickly, followed by $\psi_f(t)$ to 1 p.u. by $t = 0.15$ s. This ensures synchronization of $e_{ga}(t)$ to $u_{\infty a}$, as shown in Fig. 7(c). Furthermore, no significant start-up currents are observed after the synchronverter is physically connected to the grid at $t = 0.15$ s, as shown in Fig. 7(d).

Remark 2 (Acknowledging processor sampling time)**.** Suppose that the processor that implements the proposed controller samples at $T_s = 50$ μs, as is the case for the experimental setup in Section V. To emulate this in our simulation, we set the solution time step to be 50 μ s in PSCAD/EMTDC. Here, the synchronverter cannot achieve self synchronization if we adopt $D_f = 531$ V $\cdot$ s^2/rad as before, since this

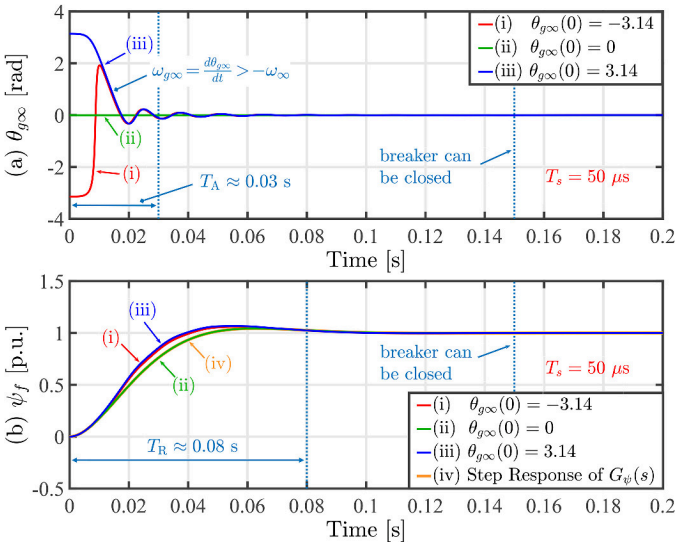

Fig. 8. Self-synchronization simulation results of the proposed controller design. Assuming that the processor sampling time is 50 μs, D_f is computed with $\eta = 0.6$.

value is computed with the assumption that T_s is much smaller. Instead, we set $\eta = 0.6$, recompute D_f according to (25) to get $D_f = 53.1$ V $\cdot$ s^2/rad. Again, we simulate the synchronverter-connected system in Fig. 2 with initial phase-angle difference $\theta_{g\infty}(0) = -3.14, 0, 3.14$ rad. Key results are shown in Fig. 8, where the phase-angle difference $\theta_{g\infty}(t)$ and the excitation flux $\psi_f(t)$, respectively, converge to 0 and 1 p.u. before $t = 0.15$ s, and we can safely close the breaker after that. Based on a visual inspection of Fig. 8(a), $\theta_{g\infty}(t)$ converges to nearly zero at approximately 0.03 s, which is expectedly greater than that observed in Fig. 7 obtained using larger value of D_f. On the other hand, note that the RPL settling time is still 0.08 s, as shown in Fig. 8(b). Thus, the use of a practical sampling time does not affect the total time needed to achieve self synchronization, which is limited by the RPL. ■

Remark 3 (Self-synchronization dynamics with LCL filter)**.** Since an LCL filter is commonly used in the synchronverter, we further validate the effectiveness of our proposed design on the LCL-filter-based synchronization design. As shown in Fig. 9, the LCL filter consists of a converter-side inductance $L_1 = 25$ mH with parasitic resistance $R_1 = 1.40$ Ω, a grid-side inductance $L_2 = 6.7$ mH with parasitic resistance $R_2 = 0.38$ Ω, and a filter capacitor $C_f = 1.4$ μF with damping resistance $R_f = 7.70$ Ω. Other system parameters remain unchanged, and the synchronverter parameters during self synchronization are recomputed as follows: $J_g = 42.0$ kg $\cdot$ m^2, $R_v = 14.3$ Ω, $D_f = 661$ V $\cdot$ s^2/rad, and $K_g = 8.92 \times 10^3$ Var $\cdot$ rad/V. We consider initial condition $\theta_{g\infty}(0) = -3.14$ rad, and plot the a-phase grid voltage u_{ta}, LCL-filter output voltage e_{Ca}, and synchronverter inner voltage e_{ga} in Fig. 10. Via visual inspection, we find that both e_{Ca} (trace (i)) and e_{ga} (trace (ii)) converge to u_{ta} (trace (iii)) before $t = 0.15$ s. Adopting the LCL filter does not impede successful self synchronization because the synchronverter controller tracks e_g to u_t and, for well tuned

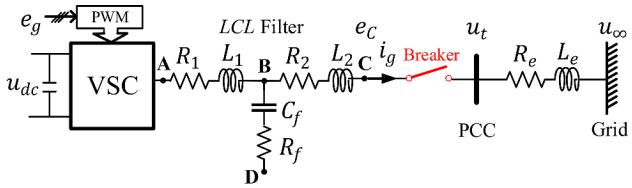

Fig. 9. Grid interface of the LCL-filter-based synchronverter.

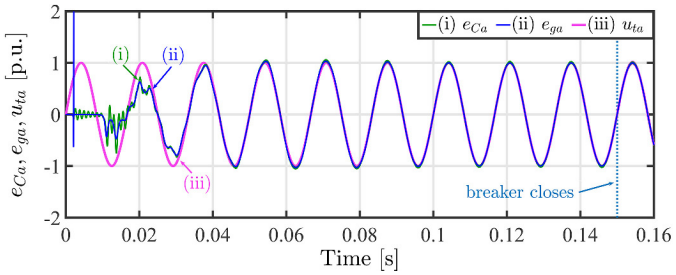

Fig. 10. Self-synchronization simulation results of the proposed controller design with an LCL filter.

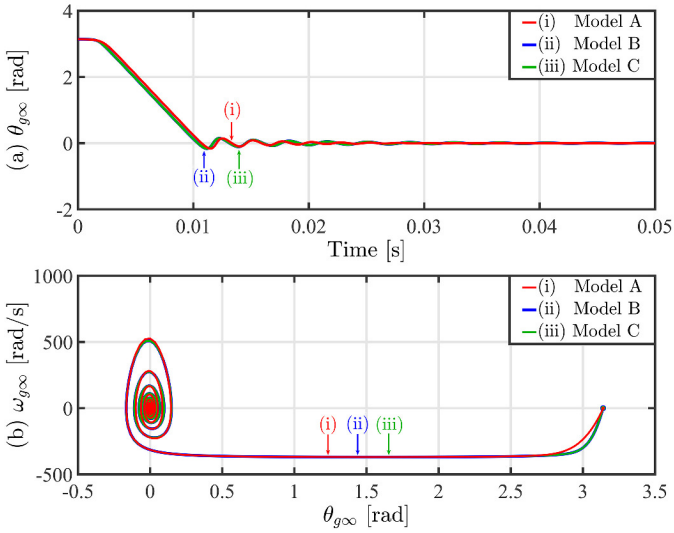

Fig. 11. Verification of the reduced second-order APL model (Model A) via comparisons with the full-order self-synchronizing synchronverter model in (9)–(14) (Model B) and Model B with (10) replaced by (29) (Model C). (a) $\theta_{g\infty}(t)$ dynamics. (b) Phase portraits ($\omega_{g\infty}$-$\theta_{g\infty}$ plots).

LCL filter, $e_C \approx e_g$ (for the fundamental-frequency component) before connection. Moreover, by comparing e_{ga} of the L-filter-based synchronverter (trace (i) in Fig. 7) and that of the LCL-filter-based synchronverter (trace (ii) in Fig. 10), we find that the two traces are nearly identical. In fact, the L- and the LCL-filter-based synchronverters achieve self synchronization with nearly identical dynamics. This is because during self synchronization, the two synchronverters can be modelled by the same full-order dynamical system, i.e., (9)–(14). As such, our analysis for self synchronization dynamics via model-order reduction and the resultant parameters to achieve fast self synchronization are valid for both L- and LCL-filter-based synchronverter designs. ■

B. Verification of Reduced Second-order APL Model

Here, we verify the suitability of the reduced second-order APL model described by (9) and (17) (Model A) developed in Section III-A as well as pertinent assumptions that lead to it. We do so by comparing the dynamics of Model A with those of the full-order synchronverter model (9)–(14) (Model B) and the full-order Model B except with (10) replaced by (29) (Model C). Note that the constant $c = 3.4$ is found via trial and error.

Simulations are conducted using Models A, B, and C with initial phase-angle difference $\theta_{g\infty}(0) = 3.14$ rad. The resulting time-domain trajectories of $\theta_{g\infty}(t)$ and phase portraits ($\omega_{g\infty}$-$\theta_{g\infty}$ plots) are depicted in Fig. 11. As shown in Fig. 11(a), the dynamics resulting from Models A (trace (i)), B (trace (ii)), and C (trace (iii)) are nearly identical. This is also observed in their respective phase portraits, as shown in Fig. 11(b). These numerical results verify that with sufficiently large D_f, replacing (10) with (29) and making Assumption 2 do not cause large modelling errors in the resultant APL dynamics, as assumed in Appendix A. Thus, the reduced second-order APL model indeed accurately captures the actual phase-angle self-synchronization dynamics.

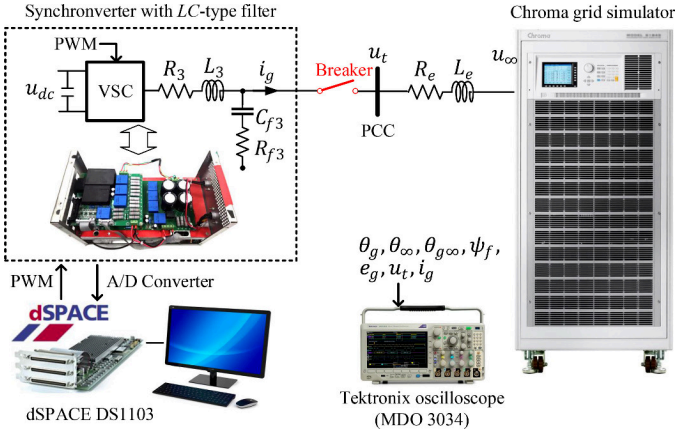

Fig. 12. Schematic diagram of self-synchronizing synchronverter experimental setup.

V. Experimental Verification

We implement the proposed self-synchronization synchronverter design experimentally via the setup shown in Fig. 12. The synchronverter is instantiated in a three-phase two-level voltage source inverter with an LC filter. The inverter switching frequency is 10 kHz. The proposed control algorithm is implemented in the dSPACE DS1103 processor board with a fixed sampling frequency 20 kHz, and the grid voltage is emulated by the Chroma 61830 grid simulator. Relevant signals are measured using the Tektronic MDO 3034 oscilloscope. System parameters are as follows: $R_3 = 0.25\ \Omega$, $L_3 = 8.0$ mH, $C_{f3} = 5.6\ \mu$F, $R_{f3} = 0.5\ \Omega$, $R_e = 0$, $L_e = 0$, $\omega_N = \omega_g^\star = \omega_\infty = 314.16$ rad/s, $U_N = U_\infty = 380$ V, $u_{dc} = 650$ V, and $S_N = 3.0$ kW. Note that due to safety considerations, we adopt a low-voltage synchronverter experimentally, but this is sufficient to validate the effectiveness of the proposed self-synchronization design.

Based on the method in [21] and (24)–(26), we choose

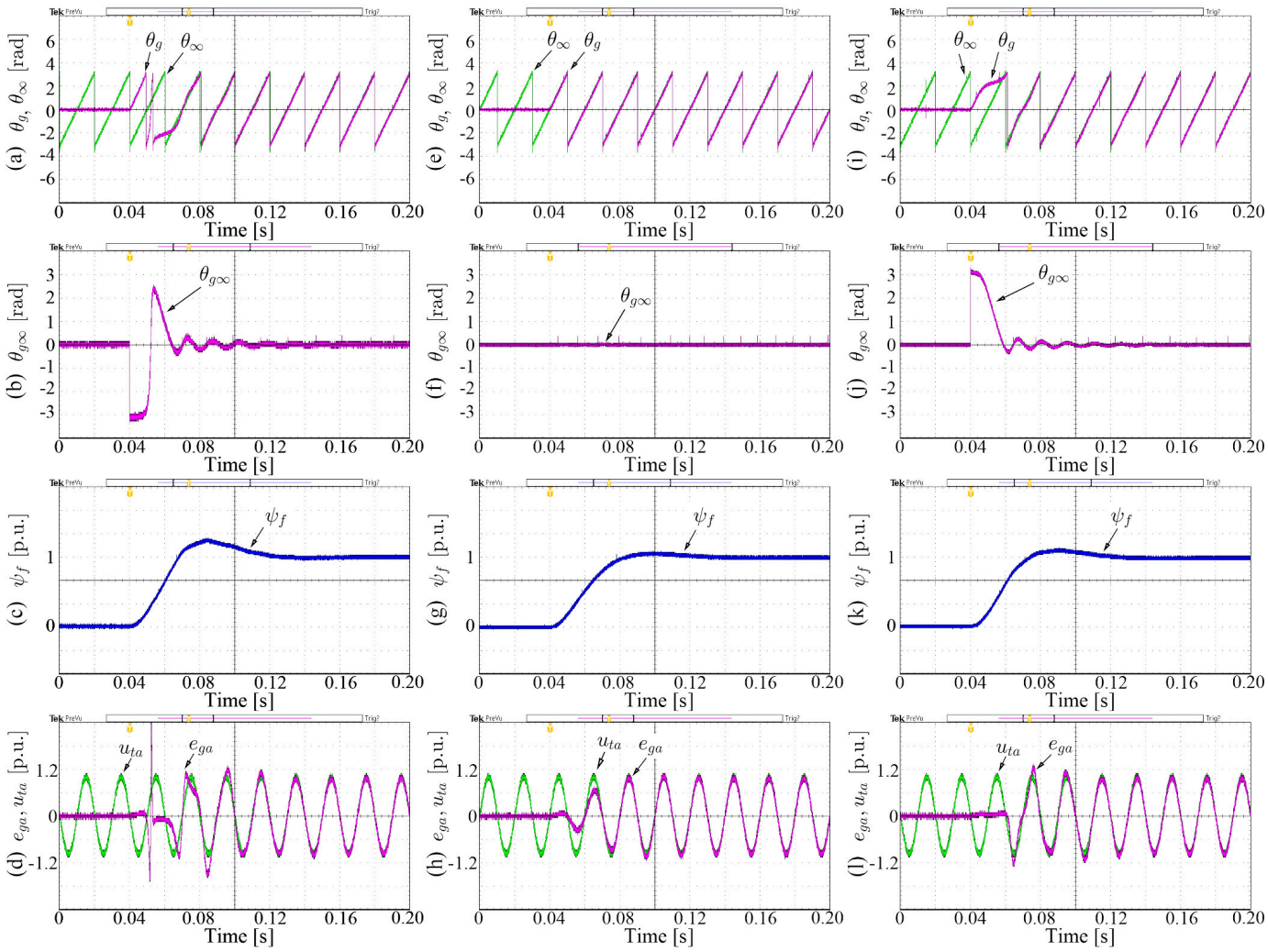

Fig. 13. Experimental results of the self-synchronization dynamics using the proposed controller design when (a)–(d) $\theta_{g\infty}(0) = -3.14$ rad, (e)–(h) $\theta_{g\infty}(0) = 0$, and (i)–(l) $\theta_{g\infty}(0) = 3.14$ rad/s.

tuneable parameters relevant to self synchronization as follows: $J_g = 0.672$ kg $\cdot$ m^2, $R_v = 7.22$ Ω, $D_f = 16.0$ V $\cdot$ s^2/rad, and $K_g = 405$ Var $\cdot$ rad/V. Similar to the simulation conducted in Remark 2, the actual sampling time $T_s = 50$ μs, so D_f is computed using (25) with $\eta = 0.6$. With the experimental setup in conjunction with the parameters above, we consider three cases in which the initial phase-angle difference $\theta_{g\infty}(0)$ is -3.14, 0, and 3.14 rad. Experimental results are shown in Fig. 13, with the self synchronization process beginning at $t = 0.04$ s, at which point the phase-angle differences $\theta_{g\infty}(t)$ in Figs. 13(b)(f)(j) start to be measured. We find that in all three cases, the proposed controller achieves self synchronization and all trajectories reach steady state within 0.15 s, similar to the simulation results in Section IV-A. Moreover, as shown in Figs. 13(c)(g)(k), $\psi_f(t)$ trajectories in all cases reach 1 p.u. with settling time 0.08 s. Also, $\psi_f(t)$ trajectories with different initial phase-angle differences are similar to each other. These observations verify our analysis in Sections III-B and III-C. Furthermore, upon closer inspection of Figs. 13(a)(b) and (i)(j), we find that $\theta_{g\infty}(t)$ converges to nearly zero approximately 0.03 s after self synchronization begins for both $\theta_{g\infty}(0) = -3.14, 3.14$ rad. This matches well with the simulations and discussion in Remark 2. We note that our observations here do not contradict those made in Example 1, since the speed of $\theta_{g\infty}(t)$ converging to zero is only slightly delayed and this small delay has little effect on the RPL response speed. In summary, the experimental results echo simulations in Section IV, and they verify the proposed self-synchronization controller, our analysis of self-synchronization dynamics, and the recommended parameter settings in (24)–(26).

VI. Concluding Remarks

This paper analyzes self-synchronization dynamics for a synchronverter design that uses only a virtual resistance (instead of both resistance and reactance) to provide active- and reactive-power feedback signals prior to grid connection. Our analyses leverage suitable reduced-order models, which are developed based on separation-of-time-scales arguments, to study the faster phase-angle and slower voltage-magnitude self-synchronization dynamics independently. The system-theoretic perspectives provide analytical justification

for the effects of controller parameters and initial conditions on self-synchronization dynamics, yield accurate estimates for self-synchronization times, and offer guidance on parameter-value settings. Compelling directions for future work include (i) adopting our proposed self-synchronization method in other VSG designs (such as the ones in [4]–[7], [22], [23]), and (ii) adopting similar model-order reduction ideas to analyze dynamics of other self-synchronizing VSG designs.

APPENDIX

A. Derivation of Reduced Second-order APL Model

During time scales that are relevant to the faster phase-angle self-synchronization dynamics, the following assertions are valid: (i) $0 < \psi_f(t) < \psi_f^\circ$ because $\psi_f(t)$ increases from $\psi_f(0) > 0$ but has not yet converged to ψ_f° (see traces marked as (ii) in Figs. 4(b) and 4(d)), and (ii) $0 < \psi_{ff}(t) < \psi_f(t)$ as the filtered signal $\psi_{ff}(t)$ is delayed compared with $\psi_f(t)$. Combining the statements above, we have that $0 < \psi_{ff}(t) < \psi_f(t) < \psi_f^\circ$. Also recall that $D_f \gg \tau_f \psi_f^\circ$ from Assumption 1. With these in mind, we get that

$$D_f \frac{\psi_f}{\tau_f \psi_{ff}^2} = \frac{D_f}{\tau_f \psi_f^\circ} \cdot \frac{\psi_f^\circ}{\psi_{ff}} \cdot \frac{\psi_f}{\psi_{ff}} \gg 1. \tag{28}$$

Thus, we can approximate (10) as

$$\begin{aligned} \frac{d\omega_{g\infty}}{dt} = &-D_f \sqrt{\frac{3}{2}} \frac{(\omega_\infty + \omega_{g\infty})\psi_f U_\infty}{J_g \tau_f \omega_N R_v \psi_{ff}} \sin\theta_{g\infty} \\ &+ D_f \frac{\psi_f}{\tau_f \psi_{ff}^2} \cdot \frac{T_{ef}}{J_g}. \end{aligned} \tag{29}$$

Furthermore, by rearranging (11) and (14), we get that

$$\sqrt{\frac{3}{2}} \frac{(\omega_\infty + \omega_{g\infty})\psi_f U_\infty}{\tau_f \omega_N R_v} \sin\theta_{g\infty} = \frac{dT_{ef}}{dt} + \frac{T_{ef}}{\tau_f}, \tag{30}$$

$$\frac{\psi_f}{\tau_f} = \frac{d\psi_{ff}}{dt} + \frac{\psi_{ff}}{\tau_f}. \tag{31}$$

Then, by substituting (30) and (31), respectively, into the first and second terms on the right-hand side of (29), and further simplifying the resultant expression, we get that

$$\frac{d\omega_{g\infty}}{dt} = -\frac{D_f}{J_g} \cdot \frac{d}{dt}\left(\frac{T_{ef}}{\psi_{ff}}\right), \tag{32}$$

where we make use of the quotient rule for derivatives. Next, by assuming that $\omega_{g\infty}(0) \approx 0$ and $T_{ef}(0) = 0$, we integrate both sides of (32) to yield

$$T_{ef} = -\frac{J_g\, \omega_{g\infty} \psi_{ff}}{D_f}. \tag{33}$$

Finally, substituting (33) into (29) and bearing in mind Assumption 2, we obtain (17), as desired. The second-order model consisting of (9) and (17) approximates the APL dynamics during phase-angle self synchronization.

B. Verifying that (25) satisfies $D_f \gg \tau_f \psi_f^\circ$

According to [21] and also used in the present work, we set

$$J_g = \frac{\sqrt{\frac{3}{2}} \psi_f^\circ U_\infty \cos\theta_{g\infty}^\circ}{{\omega_n^\star}^2 X_t (1 - 2\tau_f \omega_n^\star \zeta^\star)}, \tag{34}$$

which is valid with $D_p = 0$ as switch 2 in Fig. 2 is open. Also, by solving S_N from (24), we have

$$S_N = 0.15 \cdot \frac{U_N^2}{R_v}. \tag{35}$$

Substituting (34) and (35) into (25), we get

$$\begin{aligned} D_f &= \eta \cdot \frac{\sqrt{\frac{3}{2}} \psi_f^\circ U_\infty \cos\theta_{g\infty}^\circ}{{\omega_n^\star}^2 X_t (1 - 2\tau_f \omega_n^\star \zeta^\star)} \cdot \frac{\omega_N R_v}{0.15 U_N} \\ &\approx \frac{10\sqrt{6}\, \eta\, \omega_N \psi_f^\circ}{3{\omega_n^\star}^2 (1 - 2\tau_f \omega_n^\star \zeta^\star)}, \end{aligned} \tag{36}$$

where the approximation above results by assuming that $R_v \approx X_t$, $U_\infty \approx U_N$, and $\cos\theta_{g\infty}^\circ \approx 1$. Further suppose that the desired APL damping ratio $\zeta^\star = 0.707$ and natural frequency $\omega_n^\star \in (0, 50)$. Then the choice of $\eta \geq 0.4$ yields

$$D_f > 1.38 \psi_f^\circ \gg \tau_f \psi_f^\circ, \tag{37}$$

as desired.

C. Effect of Processor Sampling Time T_s on D_f

In practical implementation, relevant signals are sampled by the controller at fixed time period. We use the reduced-order APL model in (9) and (17) to show that the choice of D_f depends on the processor sampling time T_s. Let $\theta_{g\infty}[n] = \theta_{g\infty}(nT_s)$ and $\omega_{g\infty}[n] = \omega_{g\infty}(nT_s)$, $n = 1, 2, \ldots$ Then, the system model in (9) and (17) can be discretized as

$$\theta_{g\infty}[n] = \theta_{g\infty}[n-1] + T_s\, \omega_{g\infty}[n-1], \tag{38}$$

$$\begin{aligned} \omega_{g\infty}[n] = &\omega_{g\infty}[n-1] - \frac{T_s c}{\tau_f} \left(\alpha(\omega_\infty + \omega_{g\infty}[n-1]) \cdot \right. \\ &\left. \sin\theta_{g\infty}[n-1] + \omega_{g\infty}[n-1]\right), \end{aligned} \tag{39}$$

and successful self synchronization is achieved when its state vector $(\theta_{g\infty}[n], \omega_{g\infty}[n])$ converges to the equilibrium $x_{d1}^\circ = (2k\pi, 0)$, $k \in \mathbb{Z}$. Next, linearize the discrete APL model (38) and (39) around x_{d1}° to get

$$\begin{aligned} \begin{bmatrix} \theta_{g\infty}[n] \\ \omega_{g\infty}[n] \end{bmatrix} &= \begin{bmatrix} 1 & T_s \\ -\frac{\alpha c T_s \omega_{g\infty}}{\tau_f} & 1 - \frac{cT_s}{\tau_f} \end{bmatrix} \begin{bmatrix} \theta_{g\infty}[n-1] \\ \omega_{g\infty}[n-1] \end{bmatrix} \\ &=: A_d \begin{bmatrix} \theta_{g\infty}[n-1] \\ \omega_{g\infty}[n-1] \end{bmatrix}, \end{aligned} \tag{40}$$

with the characteristic equation $|\lambda_d I - A_d| = 0$, i.e.,

$${\lambda_d}^2 - \left(2 - \frac{cT_s}{\tau_f}\right)\lambda_d + \left(1 - \frac{cT_s}{\tau_f} + \frac{\alpha c {T_s}^2 \omega_\infty}{\tau_f}\right) = 0, \tag{41}$$

where λ_d denotes the eigenvalues of the system matrix A_d. Then, we study the impact of D_f on λ_d via the root locus analysis. To do this, we express the characteristic equation in (41) as follows:

$$1 + K \frac{1}{(\lambda_d - p_1)(\lambda_d - p_2)} = 0, \tag{42}$$

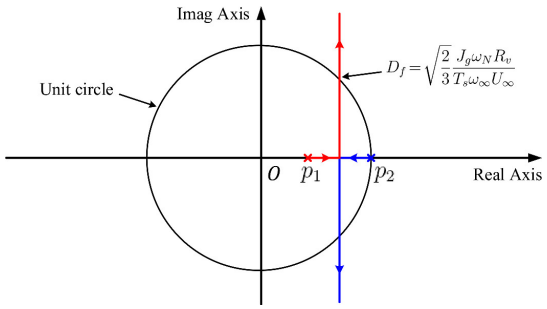

Fig. 14. Root loci patterns of the linearized discrete-time APL model in the complex plane.

where $K = \frac{\alpha c {T_s}^2 \omega_\infty}{\tau_f}$, $p_1 = 1 - \frac{cT_s}{\tau_f}$ and $p_2 = 1$. We note that K is proportional to α, and in turn D_f as well, so variations in K and D_f produce the same trends in the root loci of (42). By increasing K from 0 to $+\infty$, and also bearing in mind that $cT_s \ll \tau_f$ in practice, we obtain the root loci as shown in Fig. 14. The eigenvalues of A_d are within the unit circle only if

$$D_f < \sqrt{\frac{2}{3}\frac{J_g\omega_N R_v}{T_s\omega_\infty U_\infty}}. \tag{43}$$

In other words, though larger D_f accelerates the phase-angle self synchronization as the analysis in Section III-A shows, making D_f too large causes system instability. Moreover, according to (43), the upper limit of D_f is inversely proportional to the sampling time T_s. Thus, in practical implementations where T_s is larger, the maximum value that D_f can take before the discrete-time system becomes unstable is smaller.

D. Proof of Self-synchronization Capability

Analytical proof of successful self synchronization is necessary, since repeated simulations and experiments are valid only on a case-by-case basis and do not guarantee the self-synchronization capability of the synchronverter under all initial conditions. Here, via stability analysis, we show that the proposed design successfully achieves self synchronization for all $\theta_{g\infty}(0) \in (-\pi, \pi)$ rad (the initial value for other state variables are $\omega_{g\infty}(0) = 0$, $T_{ef}(0) = 0$, $\psi_f(0) = \psi_{ff}(0) = 0.01$, $Q_{tf}(0) = 0$, since they can be initialized in the controller). Successful self synchronization is achieved when $\theta_{g\infty}$ and ψ_f, respectively, converge to $\theta^\circ_{g\infty} = 2k\pi,\ k \in \mathbb{Z}$ ($k = 0$ in most cases), and $\psi^\circ_f = \sqrt{\frac{2}{3}}\frac{U_\infty}{\omega_\infty}$.

Since studying the dynamics of the full-order system (9)–(14) is analytically intractable, we resort to two reduced-order models, i.e., the APL model in (9) and (17) and the RPL model in (12) and (21), which capture phase-angle synchronization dynamics in the APL and voltage-magnitude synchronization dynamics in the RPL. As shown in Section III and verified in Sections IV and V, these two reduced-order models are valid for a well-tuned synchronverter.

Convergence of $\theta_{g\infty}(t)$ to zero. The set of possible initial conditions of the reduced second-order APL model in (9) and (17) is given by

$$\mathcal{B} = \{(\theta_{g\infty}, \omega_{g\infty}) \mid -\pi < \theta_{g\infty} < \pi, \text{ and } \omega_{g\infty} = 0\}. \tag{44}$$

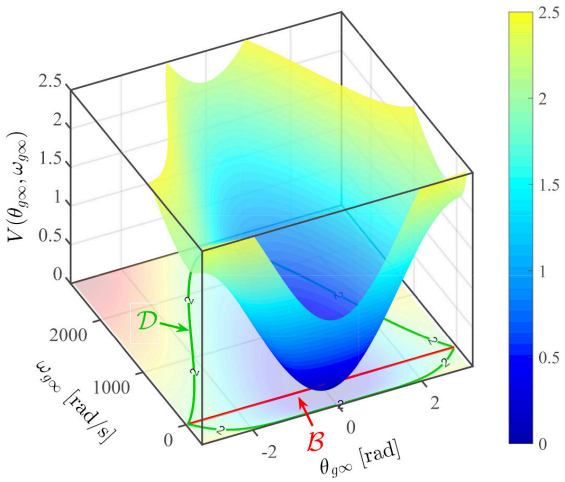

Fig. 15. Lyapunov function $V(\theta_{g\infty}, \omega_{g\infty})$ of the second-order APL model in (9) and (17).

For the system in (9) and (17), consider the Lyapunov function candidate

$$V(\theta_{g\infty}, \omega_{g\infty}) = \frac{\tau_f}{c\alpha}\left(\omega_{g\infty} + \omega_\infty \ln\left(\frac{\omega_\infty}{\omega_\infty + \omega_{g\infty}}\right)\right) + (1 - \cos\theta_{g\infty}). \tag{45}$$

As shown in Fig. 15, let

$$\mathcal{D} = \left\{(\theta_{g\infty}, \omega_{g\infty}) \;\middle|\; \begin{array}{l} -\pi < \theta_{g\infty} < \pi,\ \omega_{g\infty} > -\omega_\infty, \\ \text{and } V(\omega_{g\infty}, \theta_{g\infty}) < 2 \end{array}\right\},$$

so that $\mathcal{B} \subset \mathcal{D}$; V is positive definite in set $\mathcal{D}$, and

$$\dot{V}(\theta_{g\infty}, \omega_{g\infty}) = -\frac{\omega^2_{g\infty}}{\alpha(\omega_\infty + \omega_{g\infty})} \le 0, \tag{46}$$

for all $(\theta_{g\infty}, \omega_{g\infty}) \in \mathcal{D}$. Let $\mathcal{S} = \{(\theta_{g\infty}, \omega_{g\infty}) \in \mathcal{D} \mid \dot{V}(\theta_{g\infty}, \omega_{g\infty}) = 0\}$. Note that $\dot{V}(\theta_{g\infty}, \omega_{g\infty}) = 0$ only if $\omega_{g\infty} = 0$. Hence, $\mathcal{S} = \{(\theta_{g\infty}, \omega_{g\infty}) \in \mathcal{D} \mid \omega_{g\infty} = 0\}$, which contains only the trivial trajectory $\theta_{g\infty}(t) = 0$ and $\omega_{g\infty}(t) = 0$. To see this, consider $\omega_{g\infty} = 0$ and $\theta_{g\infty} \neq 0$, then $\frac{d\omega_{g\infty}}{dt} \neq 0$, so the trajectory will not remain within $\mathcal{S}$. Therefore, according to LaSalle's theorem (see, e.g., [20]), the origin is asymptotically stable and we conclude that all trajectories starting from initial points in set $\mathcal{B}$ converge to the origin. In other words, for a well-tuned self-synchronizing synchronverter, both $\theta_{g\infty}(t)$ and $\omega_{g\infty}(t)$ converge to zero with initial phase-angle difference $\theta_{g\infty}(0) \in (-\pi, \pi)$ rad, as desired.

Convergence of $\psi_f(t)$ to ψ°_f. The reduced-order RPL model in (12) and (21) is linear. By defining $\overline{\psi}_f = \psi_f - \psi^\circ_f$, where $\psi^\circ_f = \sqrt{\frac{2}{3}}\frac{U_\infty}{\omega_\infty}$, we get the following equivalent system:

$$\frac{d}{dt}\begin{bmatrix}\overline{\psi}_f \\ Q_{tf}\end{bmatrix} = \begin{bmatrix} 0 & -\frac{1}{K_g} \\ \sqrt{\frac{3}{2}}\frac{\omega_\infty U_\infty}{\tau_f R_v} & -\frac{1}{\tau_f}\end{bmatrix}\begin{bmatrix}\overline{\psi}_f \\ Q_{tf}\end{bmatrix}. \tag{47}$$

Also, substituting (26) into (47), we find that the eigenvalues of the system in (47) are

$$\lambda_1 = -\frac{1}{2\tau_f} + j\frac{1}{2\tau_f}, \quad \lambda_2 = -\frac{1}{2\tau_f} - j\frac{1}{2\tau_f}, \tag{48}$$

which have negative real parts. Thus, $\overline{\psi}_f(t)$ and $Q_{tf}(t)$ both converge to zero. Equivalently, ψ_f converges to $\psi_f^\circ = \sqrt{\frac{2}{3}}\frac{U_\infty}{\omega_\infty}$, as desired.

REFERENCES

[1] G. Delille, B. Francois, and G. Malarange, "Dynamic frequency control support by energy storage to reduce the impact of wind and solar generation on isolated power system's inertia," *IEEE Trans. Sustain. Energy*, vol. 3, no. 4, pp. 931–939, Oct. 2012.

[2] D. Dong, B. Wen, D. Boroyevich, P. Mattavelli, and Y. Xue, "Analysis of phase-locked loop low-frequency stability in three-phase grid-connected power converters considering impedance interactions," *IEEE Trans. Ind. Electron.*, vol. 62, no. 1, pp. 310–321, Jan. 2015.

[3] Q.-C. Zhong and G. Weiss, "Synchronverters: Inverters that mimic synchronous generators," *IEEE Trans. Ind. Electron.*, vol. 58, no. 4, pp. 1259–1267, Apr. 2011.

[4] H. P. Beck and R. Hesse, "Virtual synchronous machine," in *Proc. 9th Int. Conf. Elect. Power Quality Util.*, 2007, pp. 1–6.

[5] F. Gao and M. R. Iravani, "A control strategy for a distributed generation unit in grid-connected and autonomous modes of operation," *IEEE Trans. Power Del.*, vol. 23, no. 2, pp. 850–859, Apr. 2008.

[6] L. Zhang, L. Harnefors, and H. P. Nee, "Power-synchronization control of grid-connected voltage-source converters," *IEEE Trans. Power Syst.*, vol. 25, no. 2, pp. 809–820, May 2010.

[7] L. Huang, H. Xin, Z. Wang, K. Wu, H. Wang, J. Hu, and C. Lu, "A virtual synchronous control for voltage-source converters utilizing dynamics of dc-link capacitor to realize self-synchronization," *IEEE Trans. Emerg. Sel. Topics Power Electron.*, vol. 5, no. 4, pp. 1565–1577, 2017.

[8] Q.-C. Zhong, P. L. Nguyen, Z. Ma, and W. Sheng, "Self-synchronized synchronverters: Inverters without a dedicated synchronization unit," *IEEE Trans. Power Electron.*, vol. 29, no. 2, pp. 617–630, Feb. 2014.

[9] T. Younis, M. Ismeil, M. Orabi, M. A. Sayed, and T. Takeshita, "Single-phase virtual synchronous generator without a dedicated synchronization unit," in *Proc. 37th Int. Telecommun. Energy Conf.*, 2015, pp. 1–6.

[10] M. Karimi-Ghartemani, "Universal integrated synchronization and control for single-phase dc/ac converters," *IEEE Tran. Power Electron.*, vol. 30, no. 3, pp. 1544–1557, Mar. 2015.

[11] Q.-C. Zhong, W. L. Ming, and Y. Zeng, "Self-synchronized universal droop controller," *IEEE Access*, vol. 4, pp. 7145–7153, Oct. 2016.

[12] T. Shao, T. Q. Zheng, H. Li, and X. Zhang, "Parameter design and hot seamless transfer of single-phase synchronverter," *Elect. Power Syst. Res.*, vol. 160, pp. 63–70, Jul. 2018.

[13] W. Zhang, D. Remon, I. Candela, A. Luna, and P. Rodriguez, "Grid-connected converters with virtual electromechanical characteristics: experimental verification," *CSEE Journal of Power and Energy Systems*, vol. 3, no. 3, pp. 286–295, Sep. 2017.

[14] M. Amin, A. Rygg, and M. Molinas, "Self-synchronization of wind farm in an MMC-based HVDC system: A stability investigation," *IEEE Trans. Energy Convers.*, vol. 32, no. 2, pp. 458–470, 2017.

[15] S. Dong and Y. C. Chen, "Adjusting synchronverter dynamic response speed via damping correction loop," *IEEE Trans. Energy Convers.*, vol. 32, no. 2, pp. 608–619, Jun. 2017.

[16] J. He and Y. W. Li, "Analysis, design, and implementation of virtual impedance for power electronics interfaced distributed generation," *IEEE Trans. ind. Appl.*, vol. 47, no. 6, pp. 2525–2538, Nov. 2011.

[17] O. Mo, S. D'Arco, and J. A. Suul, "Evaluation of virtual synchronous machines with dynamic or quasi-stationary machine models," *IEEE Trans. Ind. Electron.*, vol. 64, no. 7, pp. 5952–5962, Jul. 2017.

[18] S. Dong and Y. C. Chen, "A fast self-synchronizing synchronverter design with easily tuneable parameters," in *Proc. IEEE Power Eng. Soc. General Meeting*, Aug. 2018, pp. 1–5.

[19] F. Golnaraghi and B. Kuo, *Automatic Control Systems*, 9th ed. New York: Wiley, 2010.

[20] H. Khalil, *Nonlinear Systems*. Upper Saddle River, NJ, U.S.A.: Prentice Hall, 2002.

[21] S. Dong and Y. C. Chen, "A method to directly compute synchronverter parameters for desired dynamic response," *IEEE Trans. Energy Convers.*, vol. 33, no. 2, pp. 814–825, Jun. 2018.

[22] I. Cvetkovic, D. Boroyevich, R. Burgos, C. Li, M. Jaksic, and P. Mattavelli, "Modeling of a virtual synchronous machine-based grid-interface converter for renewable energy systems integration," in *Proc. IEEE 15th Workshop Control Modeling Power Electron. (COMPEL)*, 2014, pp. 1–7.

[23] J. He, K. Wu, L. Huang, H. Xin, C. Lu, and H. Wang, "A coordinated control scheme to realize frequency support of PMSG-based wind turbines in weak grids," in *Proc. IEEE Power Eng. Soc. General Meeting*, 2018, pp. 1–5.

[24] H. Akagi, E. H. Watanabe, and M. Aredes, *Instantaneous power theory and applications to power conditioning*. Piscataway, NJ: IEEE Press, 2007.

[25] D. Remon, W. Zhang, A. Luna, I. Candela, and P. Rodriguez, "Grid synchronization of renewable generation systems using synchronous power controllers," in *Proc. IEEE Int. Conf. Renew. Energy Res. Appl.*, Nov. 2017, pp. 169–174.

[26] M. Ashabani and Y. A. R. I. Mohamed, "Integrating VSCs to weak grids by nonlinear power damping controller with self-synchronization capability," *IEEE Trans. Power Syst.*, vol. 29, no. 2, pp. 805–814, Mar. 2014.

[27] G. Zeng, T. W. Rasmussen, L. Ma, and R. Teodorescu, "Design and control of LCL-filter with active damping for active power filter," in *Proc. IEEE Int. Symp. Ind. Electron.*, 2010, pp. 2557–2562.

[28] S. H. Strogatz, *Nonlinear dynamics and chaos: with applications to physics, biology, chemistry, and engineering*. Cambridge, MA, USA: Westview Press, 1994.

[29] P. J. Antsakli and A. N. Michel, *A Linear Systems Primer*. Springer Science & Business Media, 2006.

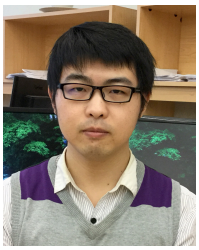

Shuan Dong (S'16) received the B.S. degree in electrical engineering from Tianjin University, Tianjin, China in 2012, and the M.S. degree in renewable energy from China Electric Power Research Institute, Beijing, China, in 2015. He is currently pursuing the Ph.D. degree in electrical engineering at The University of British Columbia, Vancouver, BC, Canada.

His research interests include HVDC technology and renewable energy integration.

Jingya Jiang (S'19) received the B.S. degree in electrical engineering from Beijing Jiaotong University, Beijing, China in 2014. She is currently pursuing the Ph.D. degree in electrical engineering at the Beijing Jiaotong University, Beijing, China.

Her research interests include renewable energy integration and power converter modelling.

Yu Christine Chen (S'10–M'15) received the B.A.Sc. degree in engineering science from the University of Toronto, Toronto, ON, Canada, in 2009, and the M.S. and Ph.D. degrees in electrical engineering from the University of Illinois at Urbana-Champaign, Urbana, IL, USA, in 2011 and 2014, respectively.

She is currently an Assistant Professor with the Department of Electrical and Computer Engineering, The University of British Columbia, Vancouver, BC, Canada, where she is affiliated with the Electric Power and Energy Systems Group. Her research interests include power system analysis, monitoring, and control. Christine is a recipient of the 2017–2018 Best Paper Award from the IEEE Transactions on Energy Conversion. She presently serves as an Associate Editors for the International Journal of Electrical Power & Energy Systems, the IEEE Transactions on Energy Conversion, and the IEEE Transactions on Power Systems.